Article

The Vertical Distribution of Ice-Nucleating Particles over the North China Plain: A Case of Cold Front Passage

Chuan He [1], Yan Yin [1,*], Yi Huang [2], Xiang Kuang [1], Yi Cui [2], Kui Chen [1], Hui Jiang [1], Alexei Kiselev [3], Ottmar Möhler [3] and Jann Schrod [4]

[1] Key Laboratory for Aerosol—Cloud—Precipitation of the China Meteorological Administration, School of Atmospheric Physics, Nanjing University of Information Science and Technology, Nanjing 210044, China; chuanhe@nuist.edu.cn (C.H.); 20171102053@nuist.edu.cn (X.K.); 001489@nuist.edu.cn (K.C.); 002829@nuist.edu.cn (H.J.)

[2] Weather Modification Office of Hebei Province, Shijiazhuang 051430, China; huangyi@hebwmo.cn (Y.H.); cuiyi@hebwmo.cn (Y.C.)

[3] Institute of Meteorology and Climate Research, Department of Atmospheric Aerosol Research, Karlsruhe Institute of Technology, Hermann Von Helmholtz–Platz 1, 76344 Eggenstein-Leopoldshafen, Germany; alexei.kiselev@kit.edu (A.K.); ottmar.moehler@kit.edu (O.M.)

[4] Institute for Atmospheric and Environmental Sciences, Goethe University Frankfurt, 60438 Frankfurt am Main, Germany; schrod@iau.uni-frankfurt.de

* Correspondence: yinyan@nuist.edu.cn

Abstract: Ice-nucleating particles (INPs) are crucial for cloud freezing processes in the atmosphere. Given the limited knowledge about the vertical distribution of INPs and its relation to aerosols in China, we present two aircraft observations of INPs over the North China Plain on 23 October 2019 and 25 October 2019, before and after a cold front passage. We used a well-established method to identify the INPs on a silicon wafer and then performed single-particle chemical composition analysis using an environmental scanning electron microscope-energy dispersive spectrometer (ESEM-EDS). The INP concentrations range from 0.1 to 9.2 L^{-1} within activation temperatures from -20 to $-29\ ^\circ$C. INPs are mostly concentrated within the boundary layer, and their concentration shows a decreasing trend with height (0.5~6 km) before the cold front passage. However, the highest INP concentration always appears at higher altitudes (4~5 km) after the cold front passage. The cold front passage also significantly weakens the correlations between the concentrations of INPs and aerosol particles at different sizes. The activated fraction (AF) of total aerosols increases from 10^{-6} to 10^{-4} with height from near ground to 6 km, reflecting a better nucleating capacity of the aerosols at higher altitudes. There is no obvious variation in AF after the cold front passage. Chemical analysis reveals that the INPs containing mineral dust components comprise the majority of total INPs during both flights. The proportion of pure mineral dust declines from 52.2% to 43.5% after the cold front passage while the proportion of mixed mineral dust increases from 23.9% to 45.7%, suggesting that an increased probability of aging or coating of INPs is introduced by the cold front during their long-distance transport. In addition, 88% of INPs have a diameter larger than 1 μm. This indicates that larger aerosols (>1 μm) are the major contributors to INPs at high altitudes despite their relatively low abundance. Our results demonstrate a significant impact of transport events on the sources and vertical distribution of INPs in the atmosphere.

Keywords: ice-nucleating particles; aircraft observation; cold front passage; vertical distribution

1. Introduction

Ice-nucleating particles (INPs) are a rare subset of aerosol particles in the atmosphere that can initiate the deposition of water vapor or the freezing of supercooled water droplets to form ice crystals [1]. INPs provide heterogeneous surfaces, making it easier for water molecule clusters to exceed a critical size for ice crystal formation compared to the homogenous nucleation process that does not involve INPs [2]. The initial formation process of ice

crystals involving INPs (i.e., heterogeneous nucleation) mainly includes four modes: contact freezing, condensation freezing, immersion freezing, and deposition nucleation [1,3]. During the first three freezing mechanisms, the ice phase forms after the supercooled droplet has formed [1]. In the final deposition nucleation mechanism, the ice phase forms directly on the surface of INPs without passing through a liquid phase [4].

In the atmosphere, only a small number of aerosols can serve as INPs and engage in the nucleation of ice crystals in clouds. Variations in INP concentrations can influence the microphysical properties of clouds, thus indirectly affecting the radiative balance of the Earth-atmosphere system [5–9]. Previous studies have demonstrated that the INP concentration is important in modulating the variation of ice crystal concentration and size within clouds, consequently exerting a significant influence on cloud morphology and lifetime [10]. Some results from global models have demonstrated that the modifications in the mixed clouds properties induced by variations in INP concentration are a significant factor contributing to the biases in radiative balance estimates in the Southern Ocean region [11]. If the INP concentration in the atmosphere increases by one order of magnitude every decade, the global net cloud radiative forcing will undergo a change of 1 W m^{-2} [12].

INP instruments can be classified into three main categories [13]. The first category involves instruments that directly measure aerosol particles, including various types of cloud chambers. These cloud chambers can be further categorized based on different measurement principles, including mixing cloud chamber [14], expansion cloud chamber [15,16] and continuous flow diffusion chamber (CFDC) [17]. These cloud chambers share a common advantage in enabling direct measurement of aerosol particles, thereby eliminating the influence of substrates and making the measurement process more representative of the actual cloud formation process in the atmosphere. The second category involves devices that measure collected particles or suspensions formed after elution on a substrate. This category includes techniques such as dry particle condensation/condensation freezing [18,19] and liquid droplet freezing devices [20–22]. These types of instruments separate the sampling and activation processes, thus making them more suitable for use in diverse sampling environments. The third category consists of single-particle/droplet suspension techniques, such as electrodynamic balance and acoustic levitation, which can be used to measure individual particles or droplets [23,24]. Different instruments may produce certain differences in measurement results due to their different principles. For example, within the temperatures from −12 to −38 °C, results from 17 different ice nucleation instruments for illite, a type of mineral, showed measurement discrepancies exceeding a factor of 1000 at the same activation temperature [25]. Clearly, the measurement of INP concentrations still involves significant uncertainty. The accuracy and errors of measurements from different types of instruments require further assessment and calibration.

The sources of INPs in the atmosphere are complex, including natural sources such as deserts and ocean emissions, as well as anthropogenic sources such as traffic, industrial activities, and biomass burning. The INPs from different sources may exhibit distinct ice-nucleating capacities due to differences in their chemical compositions [26]. Mineral dust emissions are substantial on a global scale and exhibit remarkable ice-nucleating capacity, especially at temperatures below −17 °C [27–30]. The surface properties of mineral dust particles can greatly affect their ice-nucleating capacity. Enlarging the particle size can increase the number of activation sites on the surface of particles, making ice activation more likely to occur [31,32]. The physical and chemical processes that occur during transport may also potentially modify the ice-nucleating capacity of dust. Some studies suggested that the aging process of mineral dust during long-distance transport can enhance their ice-nucleating capacity, although further observations are required to validate this conclusion [33]. Biological aerosols are considered another widely present type of INPs [34–36]. Biological aerosols can activate at relatively higher temperatures, even though their global emissions are much lower than those of mineral dust [37]. Additionally, some aerosols originating from anthropogenic emissions, such as organic aerosols [38] and black carbon [39], can also serve as INPs. Recent studies revealed that secondary

organic aerosols (SOA) have good ice-nucleating capacity under cirrus cloud condition but do not act as INPs under mixed-phase cloud conditions [40,41]. Compared to pristine natural aerosol particles, the ice-nucleating capacity of natural aerosols coated with SOA is weaker [42,43].

Over the past decades, a large number of field observations of INPs have been carried out around the world. INP concentrations vary significantly from region to region and are sensitive to the underlying surface conditions, meteorological conditions, and the altitude of the sampling sites [30,44]. Schneider reported the seasonal variability of INP concentrations in northern forests of Finland, and average INP concentrations in summer were four times higher than those in winter [22]. Chou's research demonstrated that Saharan dust events led INP concentrations increasing by more than two orders of magnitude [45]. Typically, INP concentrations show a significant correlation with the concentrations of aerosol particles exceeding 0.5 μm in size [46–49], although there have been a few studies that found no relationship between INP concentrations and aerosol concentration [21,50]. There were also some INP observational studies conducted in China in recent years. Observations in mountainous areas indicated that mineral dust is the most effective INP in spring, while anthropogenic aerosol pollution has a limited contribution [51]. Winter observations in Beijing revealed that the mountainous region exhibits a higher abundance of INPs that can be activated at higher temperatures compared to the central urban region [52]. Summer observations in Beijing indicated that INP concentrations in the atmosphere did not show a clear trend of increase or decrease during the pollution events [53]. Zhang's research also confirmed the negligible influence of anthropogenic black carbon and secondary aerosols emissions on INP concentrations [54]. However, Ren's results showed that the INP concentrations gradually increased as aerosol conditions transitioned from clean to heavy pollution [55]. Therefore, further investigations are still required to understand the INPs sources and its influencing factors in China.

Given that clouds in the natural environment form at high altitudes, the vertical profiles of INP concentrations are a crucial issue in INP research [56]. However, until now, there has been no consistent conclusion on the distribution of INPs in the actual atmosphere at high altitudes. Various factors, including aerosol composition, weather conditions, atmospheric state, and underlying surface conditions, can influence INP concentrations at high altitudes [56]. Some studies found that there is almost no difference in INP concentrations from near ground up to an altitude of 5 km [57,58]. But aircraft observations in India revealed significant variations in INP concentrations within the same altitude range, with notably higher INP concentrations observed at altitudes below 3 km [59]. Results from Twohy [60] and Conen [61] indicated a decrease in INP concentrations with increasing altitude, with INPs primarily contributed by biogenic aerosols. Paul et al. found an increasing trend in INP concentrations with increasing altitudes (below 3.6 km) through aircraft observations [62]. There are also limited field observations regarding the INP vertical profile in China. Observations at different altitudes on Mt. Huang showed that the INP concentrations at the summit were significantly lower than those at the base of the mountain [63]. Aircraft observations over the Helan mountain region [64] and Shenyang [65] also indicated a decreasing trend in INP concentrations with increasing heights, and artificial seeding affected INP concentrations at cloud tops. Observations in Xinjiang found that the inversion layer near the boundary layer inhibited the vertical transport of aerosol particles, thus affecting the vertical distribution of INP concentrations [66]. Aircraft observations carried out in Xingtai and Shijiazhuang [56] showed that larger particles (>0.5 μm) in the upper troposphere exhibited a better ice-nucleating capacity compared to those near the surface. However, the chemical composition of INPs at high altitudes remains unclear.

INPs emitted from sources over China play a vital role in global INP estimates. However, given the notable lack of observational data on INPs at high altitudes in China, the concentrations and chemical composition of INPs at different altitudes remain unclear. Aircraft INP observations are of great significance for investigating the sources and vertical distribution of INPs in China, especially for studying the impact of transport processes

on INP concentrations at higher altitudes. This study presents aircraft-based observations of INP vertical distributions over Shijiazhuang (SJZ, an industrial city in the North China Plain) on 23 October 2019 and 25 October 2019. This is a unique case study where two flight missions were conducted before and after the passage of a cold front. The influences of transport processes on the vertical distribution of INPs were examined. We employed a well-established method to identify activated INPs on the substrate and performed single-particle chemical composition analysis using environmental scanning electron microscopy (ESEM). This approach provides more convincing evidence for understanding the sources of INPs from the near surface to high altitudes. This paper is arranged as follows: materials and methodology used in aircraft observations and INP measurements are elucidated in Section 2; detailed results of field measurements are presented in Section 3; the comparison between our results and those from previous studies is discussed in Section 4; conclusions are listed in Section 5.

2. Materials and Methods

2.1. Sampling Site and Flight Routes

Two aircraft observations were carried out over SJZ (114.6°E, 38.1°N) in the North China Plain (Figure 1) on 23 October and 25 October 2019, with a two-day interval. During these two days, a cold front passed over the North China Plain. A detailed weather conditions analysis is shown in Section 3.1. SJZ is located in the central region of the North China Plain and is often affected by Mongolian cyclones and Siberian cold air in spring. The climate over SJZ region can be characterized by rare rainfall, which occurs mostly during the summer, and prevalent wind. SJZ is one of the most densely populated cities in China, with a population of over 10 million. The substantial population and the presence of numerous industrial facilities within the city contribute to the complex sources of aerosol particles within the boundary layer over SJZ, including traffic emissions, industrial emissions, biomass burning, and dust generated by construction activities.
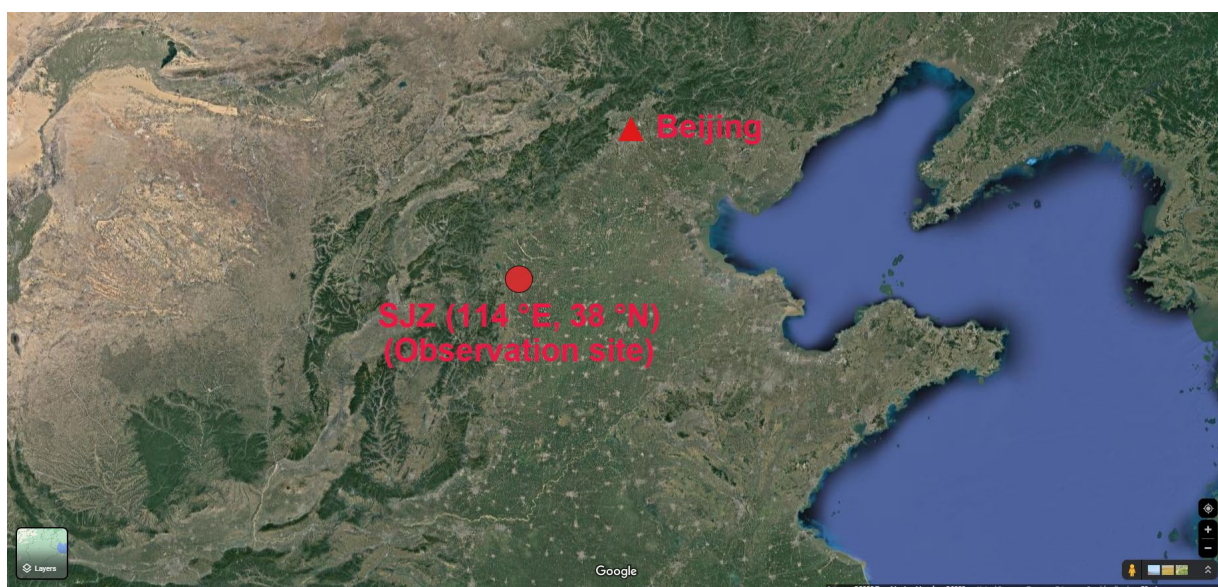

Figure 1. The location of observation site (http://www.google.com/maps (accessed on 8 August 2023)).

Situated approximately 30 km from SJZ, Zhengding Airport served as the launch site for both flights. The take-off time was around 8:00 p.m. local time. After ascending to an altitude of 5.4 km, the aircraft performed a spiral descent over SJZ (Figure 2). The aircraft stabilized at the same altitude for approximately 10 min after descending 600 m during each spiral descent to facilitate the collection of aerosol samples. It should be noted that, during the first flight, the minimum altitude at which the aircraft spiraled over SJZ was

600 m, while during the second flight, it was 2.1 km. This discrepancy in minimum altitudes resulted from specific restrictions imposed during the second flight that prohibited the aircraft from flying below 2 km.
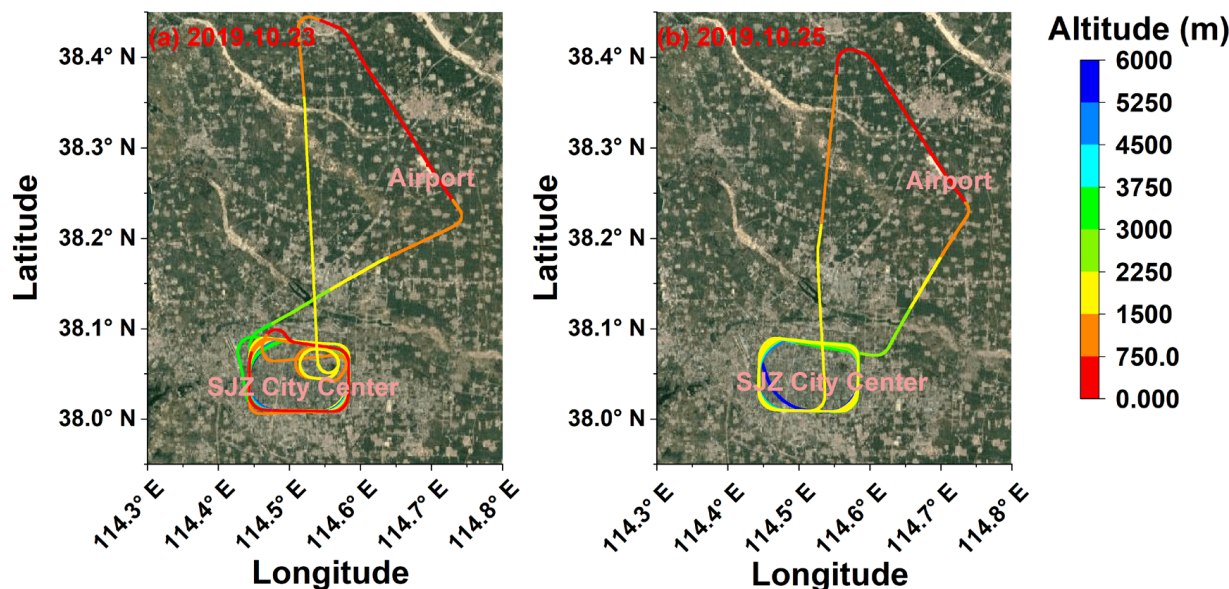

Figure 2. Flight trajectories on 23 October 2019 (**a**) and 25 October 2019 (**b**).

2.2. Sampling and Measurement of Aerosols

A King-air aircraft was instrumented and operated to collect aerosol samples. Throughout the whole flight, ambient air containing aerosol particles was pumped into the aircraft. These particles were drawn in via an isokinetic inlet and subsequently directed to diverse instruments. An isokinetic sampling technique was adopted to prevent undesirable thermal effects on aerosol concentration and composition. A high-voltage electrostatic aerosol collector (HVEAC) was installed on the aircraft to collect INP samples. There was no specific size cut-off for either isokinetic inlet or HVEAC. The isokinetic inlet and HVEAC exhibited a collection efficiency of about 90% and 60% for particles smaller than 10 μm, respectively. Their collection efficiency decreased to some extent for particles lager than 10 μm. Considering the particle loss during collection, the concentrations of particles larger than 10 μm in the aerosol samples were lower than those in the real ambient atmosphere. These samples were subsequently analyzed in a well-established static vacuum water vapor diffusion cloud chamber [56,63,67]. For each sample, ambient air was pumped at a constant rate of 2 L per minute for 5 min by HVEAC. These particles possessed a negative charge and subsequently transported to the positively charged surface of a 45 mm silicon wafer, where they underwent deposition. It is noted that each sample was collected during the aircraft's first circular flight at a constant altitude, which helps avoid potential contamination from aircraft exhaust emissions to some extent. A total of 19 samples were collected during these two flights.

To obtain the size distribution of aerosol particles during the flight, we used a passive cavity aerosol spectrometer probe (PCASP) to measure the concentration of aerosol particles in the size range from 0.1 to 3.0 μm (with a time resolution of 1 s). In addition, aircraft integrated meteorological measurement (AIMM-20) was utilized to measure wind speed and direction, the position parameters of aircraft, as well as the ambient temperature and relative humidity.

2.3. INP Analysis

All the collected samples were stored in sealed containers and subsequently transported to the laboratory. An INP analysis chamber, called a static vacuum water vapor diffusion chamber, was established at Nanjing University of Information Science & Tech-

nology [68]. This chamber was designed based on the fundamental principle of FRIDGE (Frankfurt Ice Nuclei Deposition Freezing Experiment) [67]. A brief description of this chamber is given below.

The main body of this diffusion chamber consists of the activation chamber and water vapor chamber, each equipped with pressure gauges and Peltier-cooled plates. The activation chamber system was evacuated using a vacuum pump before each activation experiment to allow water vapor to diffuse into the activation chamber and to avoid potential contamination by particles present in the laboratory air. Based on the pressure and temperature (T) measurements in both chambers, we derived the relative humidity (RH) on the surface of silicon wafer during the activation of ice crystals. The valve connecting these two chambers was opened when the T and RH of both chambers reached the value we had set, allowing water vapor to be introduced into the activation chamber, thus activating the ice crystals. During each activation experiment, a CCD camera continuously monitored the growth of the ice crystals for 100 s, which was sufficient to activate all INPs. The software provided with the instrument automatically counted the number of ice crystals. Note that the number of ice crystals gradually increased during the first 30 s after opening the valve; after that, the ice crystals continued to grow but no new ice crystals appeared.

At each temperature (-20 °C, -23 °C, -26 °C, and -29 °C ($\sigma = \pm 0.1$ °C)), aerosol samples were analyzed at relative humidity with respect to water (RH_w) of 95, 97, 99, and 101%, which is equivalent to 110–135% with respect to ice (RH_i) (Table 1). The uncertainty of RH_i falls within the range of 0.4–0.6%. Detailed methods for calculating the uncertainty of RH_i are provided by Jiang [53]. In addition, a clean silicon wafer washed with chromic acid was used as a blank control for the activation experiment, and almost no ice crystals were activated on the blank control.

Table 1. Activation temperatures and relative humidity at which INPs are analyzed.

T (°C)	RH_w (%)	RH_i (%)
-20	95	115.6
	97	118.0
	99	120.4
	101	122.9
-23	95	119.0
	97	121.5
	99	124.0
	101	126.5
-26	95	122.5
	97	125.1
	99	127.7
	101	130.2
-29	95	126.2
	97	128.8
	99	131.4
	101	134.0

2.4. Chemical Analysis

There are three marked crosses engraved on the edges of silicon wafer. A coordinate system is established by these crosses to locate the ice crystals and INPs in the pictures taken by the CCD camera. Selected samples (11/19) were reactivated in the FRIDGE instrument (Goethe University in Germany, Frankfurt, Germany) to obtain pictures containing the engraved crosses and ice crystals (Figure 3a). The structure of the static vacuum water vapor diffusion chamber is basically the same as the FRIDGE instrument, and the INP concentrations measured by these two instrument are very close (within $\pm 5\%$ at the same activation temperature and RH). Therefore, the influence of reactivation experiments on subsequent INP analysis is negligible. These samples were subsequently analyzed using an

environmental scanning electron microscopy–energy dispersive spectrometer (ESEM-EDS, FEI Quanta 650 FEG) to investigate the elemental composition and morphology of INPs. There is a new coordinate system in the ESEM. The transformation matrix between these two coordinate systems (in the ESEM and in the pictures taken by the CCD camera in FRIDGE) can be calculated by locating the three marked crosses. In this way, the coordinates of ice crystals in the pictures taken by the CCD camera can be converted into coordinates in the ESEM system. Given the abundance of aerosol particles on the silicon substrates in the ESEM system, if more than one particle is present at a location where an ice crystal has appeared, we excluded these particles from our INP database. We identified a particle as an INP only if it is the only particle present at the location where an ice crystal has appeared. We scanned the positions of over 300 ice crystals using the ESEM system, but only 93 particles could be identified as INPs. An example of an identified INP is shown in Figure 3b.
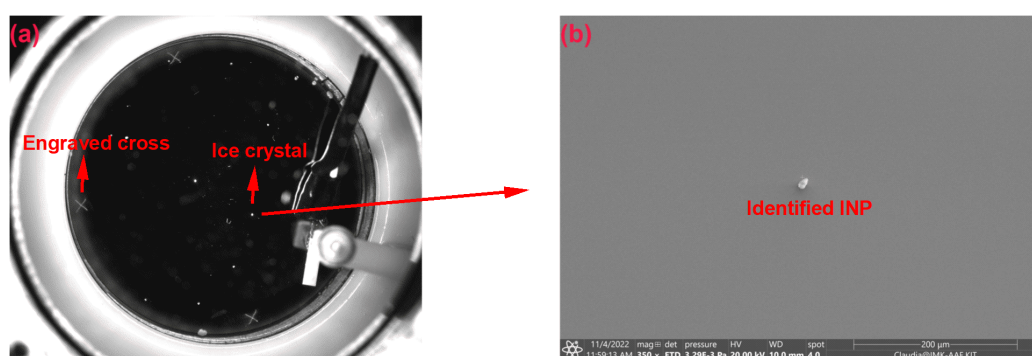

Figure 3. Representative images of ice crystals in cloud chamber (**a**) and identified INP in ESEM system (**b**).

All the INPs are manually classified into six categories based on their elemental composition. These categories include pure mineral dust, dust mixed with biogenic material, dust mixed with organic material, pure biogenic material, pure organic material, and aluminum rich material. It should be noted that the substrates used for aerosol sampling are made of silicon, so the silicon signal was excluded from the subsequent chemical classification analysis. Aluminum was used as a representative element to define the composition of mineral dust components, nitrogen (containing phosphorus/sulfur/potassium as well) was used to define the composition of biogenic components, carbon and oxygen were used to define the composition of organic components. The detailed classification schematic is shown in Figure 4.
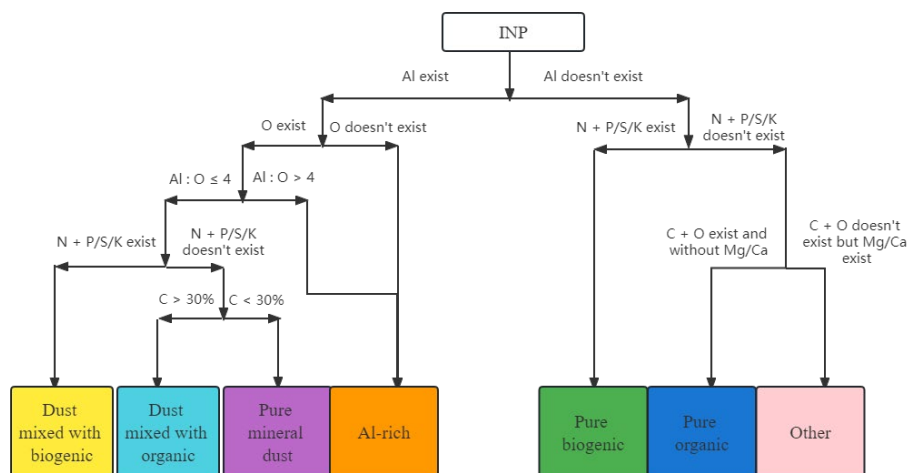

Figure 4. Classification schematic of INPs.

2.5. Back Trajectories of Air Masses

Back trajectories of the air masses were calculated using NOAA's Hybrid Single-Particle Lagrangian Integrated Trajectory model (HYSPLIT) [69] with $1° \times 1°$ GDAS data. The HYSPLIT trajectory model is widely used for investigating the origin, transport pathways, and dispersion patterns of air masses, aerosols, and various pollutants.

3. Results

3.1. Weather Condition Analysis

The two flights were conducted before and after a cold front passage. Figure 5 shows the mean sea level pressure and 1000 hPa wind fields at 2:00 p.m. local time on 23 October 2019 and 25 October 2019. On 23 October, the center of the Mongolian high-pressure system was located near 50°N latitude. The surface cold front was situated in the central region of Inner Mongolia, extending roughly in a west-southwest to east-northeast direction. The SJZ area was located within the prefrontal pressure field of the cold front, experiencing the influence of a relatively weak southerly wind. On 25 October, the surface cold front had moved out of the North China Plain. The SJZ area was subsequently influenced by post-frontal cold high pressure, resulting in reduced surface wind speeds and predominantly northerly wind. Vertical profiles of ambient relative humidity and temperature before and after the cold front passage are shown in Figure 6. It is evident that after the cold front passage, there was a notable decrease in both ambient temperature and relative humidity along the vertical direction. Specifically, surface temperatures decreased from 15 °C to 10 °C and relative humidity decreased from 80% to 50%, indicating that the cold front brought dry and cold air to the SJZ area.
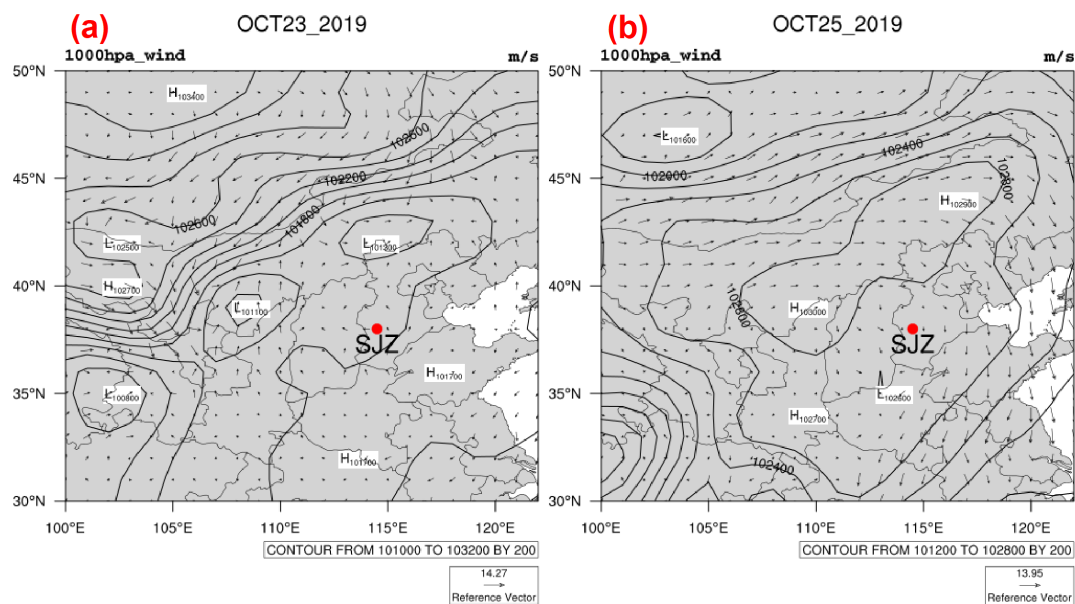

Figure 5. The mean sea level pressure and 1000 hPa wind fields at 2:00 p.m. local time (UTC + 8) on 23 October 2019 (**a**) and 25 October 2019 (**b**).

The 36-h HYSPLIT back trajectories at starting heights every 500 m from 0.5 to 5 km, calculated for observation periods before and after the cold front passage, are shown in Figure 7. Before the cold front passage, air masses above 4 km predominantly originated from the northwest and relatively closer regions, whereas those below 4 km originated from the southern direction. After the cold front passage, air masses at starting heights of 0.5~5 km all originated from the northwest direction and from more distant regions. Specifically, air masses above 4 km originated from Xinjiang, a very distant region that includes the Taklamakan Desert, the largest desert in Asia, and the Mongolian Gobi Deserts.
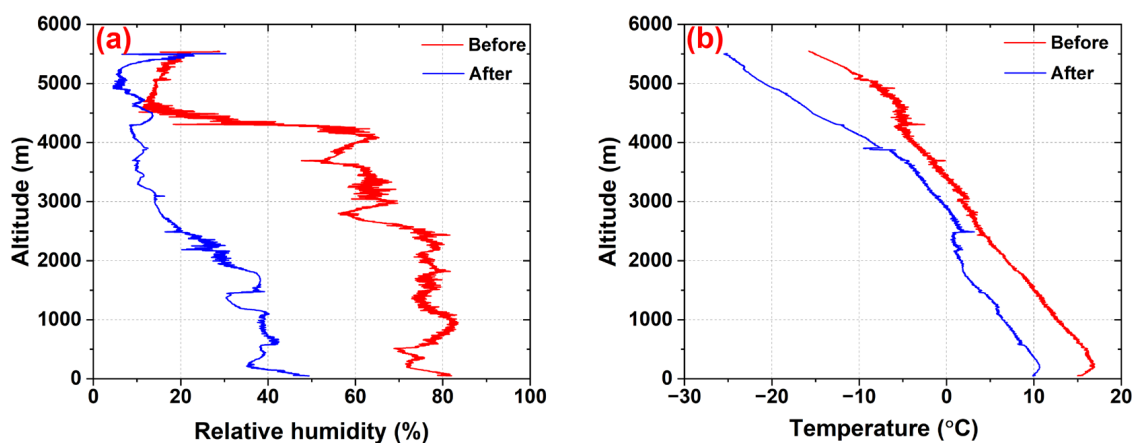
Figure 6. The vertical distribution of ambient relative humidity (**a**) and temperature (**b**) before (red line) and after (blue line) the cold front passage.
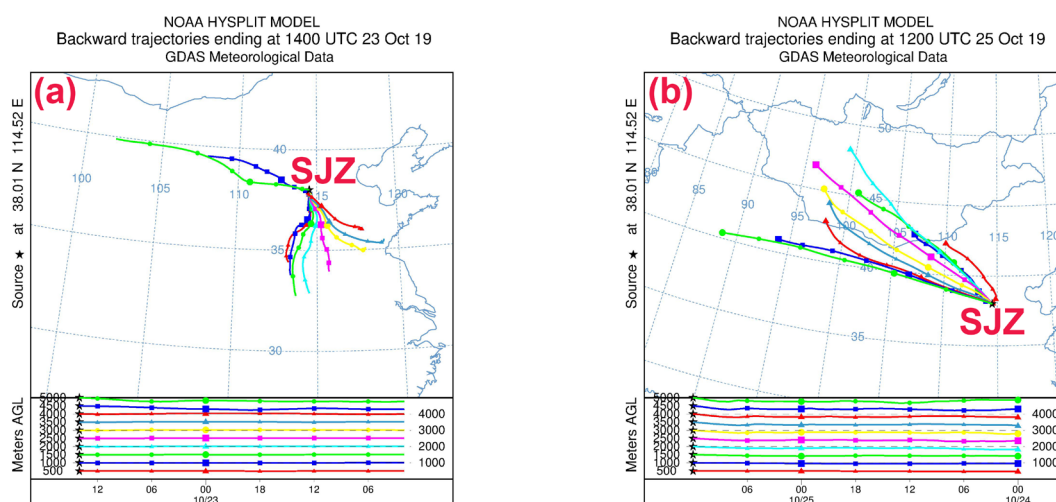

Figure 7. 36 h back trajectories calculated at starting heights every 500 m from 0.5 to 5 km for observation periods before (**a**) and after (**b**) the cold front passage using HYSPLIT.

3.2. INP Measurements

This study focuses on the deposition and condensation freezing modes among the four heterogeneous nucleation modes. Each aerosol sample was analyzed at the activation temperature −20, −23, −26, −29 °C and RH_w of 95, 97, 99, 101%, which is equivalent to RH_i of 110–135%, to obtain INP number concentrations. Table 2 summarizes the average, minimum, and maximum INP concentrations during the observations. Within the temperature range of −20~−29 °C, the INP concentrations vary from 0.1 to 9.2 L^{-1}. Even at a given temperature, the INP concentrations experience variations exceeding a factor of 10. At −20 °C, it is common to observe a significantly reduced occurrence of activated ice crystals, or even the absence of ice crystals. Therefore, identifying a trend from INP concentrations analyzed at −20 °C is not feasible. At a constant RH_w, INP concentrations increase with the decreasing temperature. Similarly, at a constant temperature, INP concentrations generally increase with the increase of RH_w, but this trend is not as obvious at very low concentrations (near 0). The average INP concentrations at −26 and −29 °C are higher before the passage of the cold front compared to the concentrations after its passage. This could be attributed to the fact that no samples were collected at lower height (<2 km) during the flight after the cold front passage. Aerosol concentrations at lower height, particularly within the boundary layer, are much higher than those at higher altitudes, making a greater contribution to INP concentrations (as discussed in Section 3.3).

Table 2. The statistical concentration of INPs before and after the cold front passage.

T and RH$_w$		Minimum N$_{INP}$ (L^{-1})		Maximum N$_{INP}$ (L^{-1})		Average N$_{INP}$ (L^{-1})		±Standard Deviation of Average (L^{-1})	
		Before	After	Before	After	Before	After	Before	After
−20 °C	95%	0.0	0.0	0.2	0.5	0.1	0.1	0.056	0.164
	97%	0.0	0.0	0.2	0.6	0.1	0.2	0.072	0.192
	99%	0.1	0.1	0.3	0.7	0.2	0.3	0.074	0.212
	101%	0.1	0.2	0.3	0.9	0.3	0.4	0.084	0.242
−23 °C	95%	0.1	0.1	0.4	0.6	0.2	0.2	0.082	0.166
	97%	0.1	0.2	0.4	0.8	0.3	0.4	0.068	0.184
	99%	0.3	0.3	0.8	1.0	0.5	0.6	0.134	0.244
	101%	0.3	0.4	1.1	1.3	0.7	0.8	0.214	0.33
−26 °C	95%	0.6	0.5	1.5	1.2	1.0	0.7	0.224	0.31
	97%	0.8	0.4	1.8	1.3	1.3	0.9	0.302	0.316
	99%	1.1	0.6	2.3	1.5	1.5	1.1	0.358	0.318
	101%	1.2	0.8	2.5	1.8	1.8	1.3	0.476	0.348
−29 °C	95%	2.0	0.9	5.8	3.6	3.9	2.5	1.308	0.894
	97%	2.5	1.2	6.7	3.9	4.3	2.8	1.404	0.936
	99%	3.0	1.5	7.9	4.4	4.9	3.2	1.682	0.95
	101%	3.6	2.0	9.2	4.9	5.7	3.7	1.922	0.928

3.3. Verticlal Profile of INP and Aerosol Concentration

Previous research has indicated a strong correlation between the concentration of aerosol particles (with a diameter larger than 0.5 µm) and INP concentration [32,46,56]. Figure 8 shows the flight trajectories with concentrations of total particles and particles exceeding 0.5 µm in diameter during the flights before and after the cold front passage. During both flights, high aerosol concentration values were primarily concentrated within the boundary layer. The aerosol concentration rapidly decreases by 1 order of magnitude from a height of 2~3 km, which is more obvious during the flight before the cold front passage (Figure 8a,c). The cold front passage significantly reduces the total aerosol concentration within the boundary layer, as well as the concentration of larger aerosols. However, this reduction is not as significant above 3 km, with even a slight increase in the concentration of larger aerosols (>0.5 µm) above 3 km after the cold front passage. In general, the cold front passage did not modify the overall trend of decreasing aerosol concentration with height. However, it did lead to significant differences in its impact on aerosol concentration at different heights (below and above boundary layer).

Given the limitations in observation methods and instruments, the profile of INP concentration is highly scarce within the global INP measurement database. Here, we present the vertical distributions of INP concentrations (T = −20, −23, −26, −29 °C and RH$_w$ = 99%) before and after the cold front passage (Figure 9). INP concentrations show almost no correlation with height at higher activation temperatures, especially at −20 °C, which is due to the near-zero values of the INP concentrations (as discussed in Section 3.2). At lower activation temperatures (T = −26, −29 °C), INPs are mostly concentrated within the boundary layer before the cold front passage, and the INP concentration has a decreasing trend with height. These high values within the boundary layer may explain the overall higher average INP concentrations of all samples before the cold front passage compared to after the passage (as mentioned in Section 3.2). After the cold front passage, the INP concentrations do not exhibit a decreasing trend with heights. On the contrary, the highest value always appears at higher altitudes (4~5 km). Shifts in the vertical distribution of INP concentration partly explain the weakened correlation between INP concentration and aerosol number concentration after the cold front passage (Table 3). Before the cold front passage, the INP concentrations correlated well with concentration of particles with different sizes (larger than 0.2, 0.3, 0.4, and 0.5 µm), as both INP concentration and aerosol

concentration exhibited a similar trend that decreased with height. The correlations weakened after the cold front passage, likely due to the variations in vertical distribution of INP concentrations.
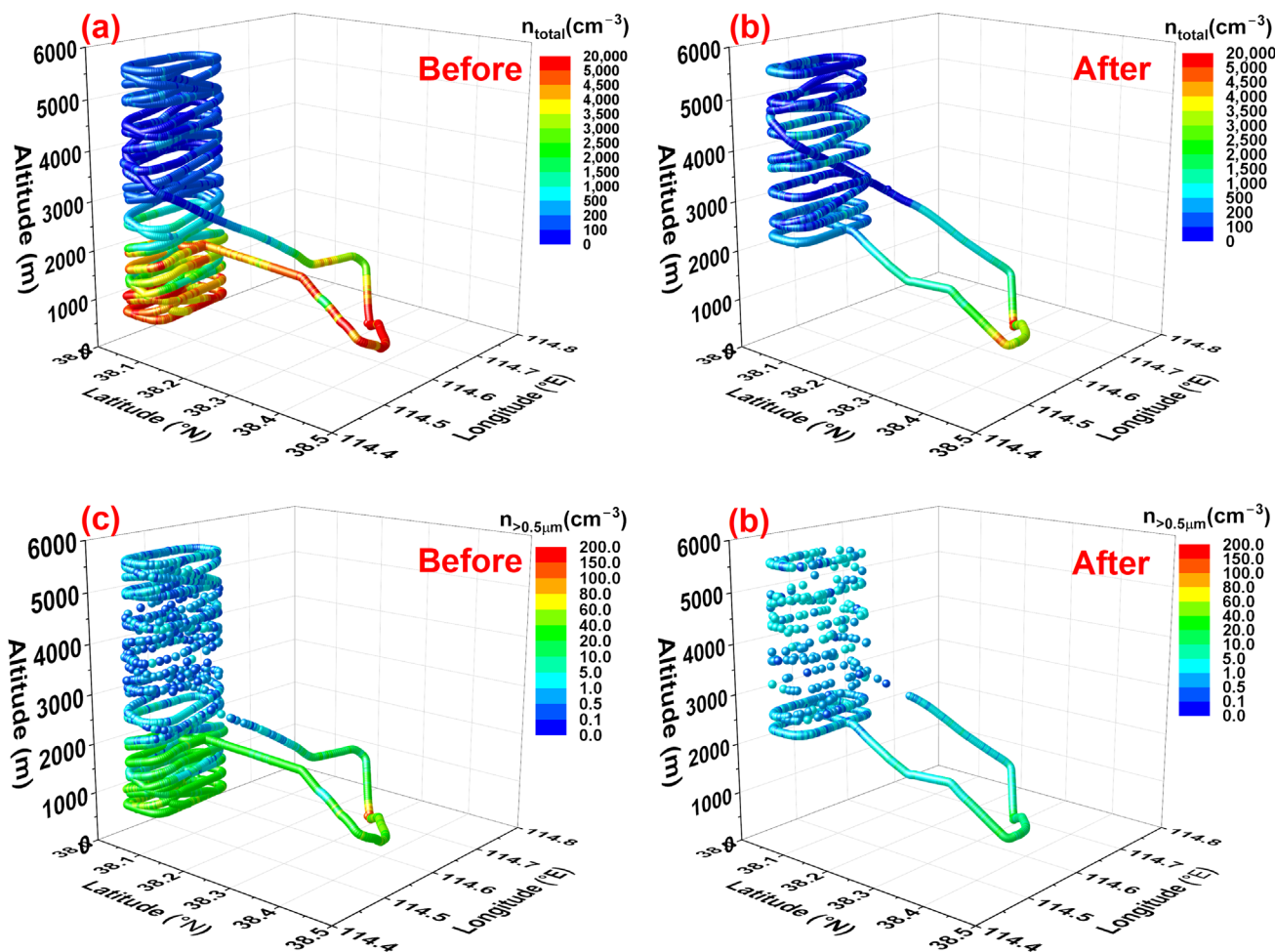

Figure 8. Flight trajectories with concentrations of total particles and particles exceeding 0.5 μm in diameter during the flights before (**a**,**c**) and after (**b**,**d**) the cold front passage.

Table 3. The correlation (R^2) and significance level (P) between INP concentration and aerosol concentration before and after the cold front passage.

Aerosol Size	N_{INP} before the Cold Front Passage		N_{INP} after the Cold Front Passage	
	R^2	P	R^2	P
Total particles	0.55	0.190	0.18	0.448
D > 0.2 μm	0.47	0.164	0.06	0.689
D > 0.3 μm	0.43	0.179	0.05	0.767
D > 0.4 μm	0.49	0.152	0.04	0.325
D > 0.5 μm	0.49	0.189	0.03	0.599

Figure 10 presents the activated fraction (AF) of total aerosols at different heights before and after the cold front passage. Before the cold front passage (Figure 10a), the AF increases significantly from 10^{-6} to 10^{-4} from near ground to 6 km. This increase is attributed to the substantial decrease (orders of magnitude) in aerosol concentration with height, while the INP concentrations remain within the same order of magnitude. The increase in AF indicates a better nucleating capacity of the aerosols at higher altitudes, despite much lower total particle concentrations than near ground. In addition, there is no obvious variation in AF after the cold front passage. This is because the cold front does not

lead to order-of-magnitude variations in either aerosol concentration or INP concentration at the height of 2~6 km.
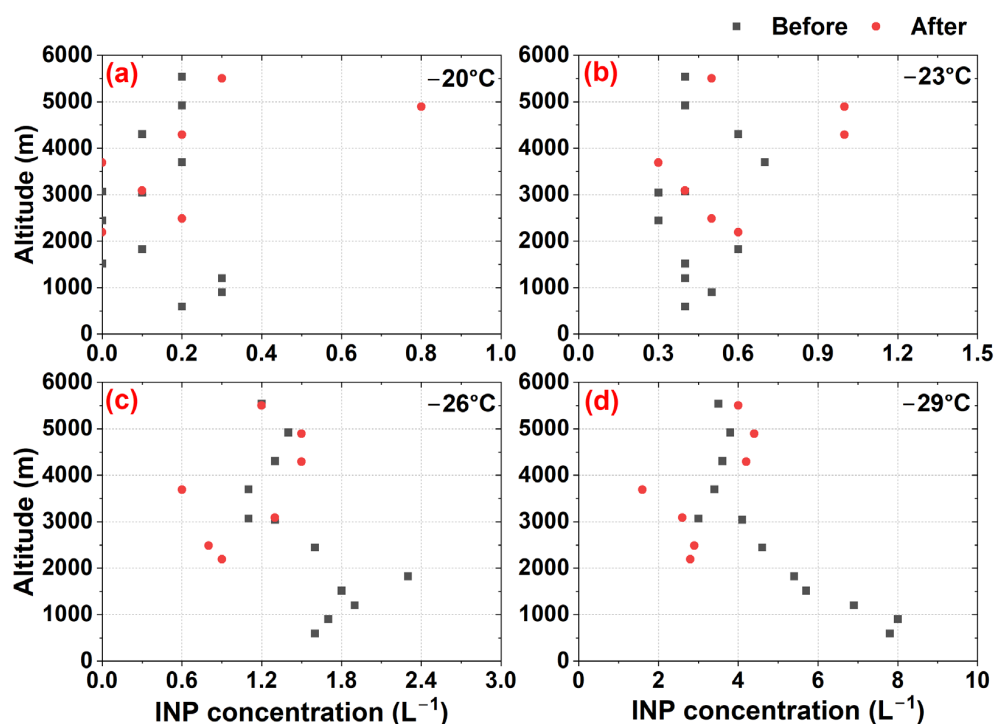

Figure 9. Vertical distribution of INP concentration (RHw = 99%) at activation temperature of −20 °C (**a**), −23 °C (**b**), −26 °C (**c**) and −29 °C (**d**) before (black dots) and after (red dots) the cold front passage.
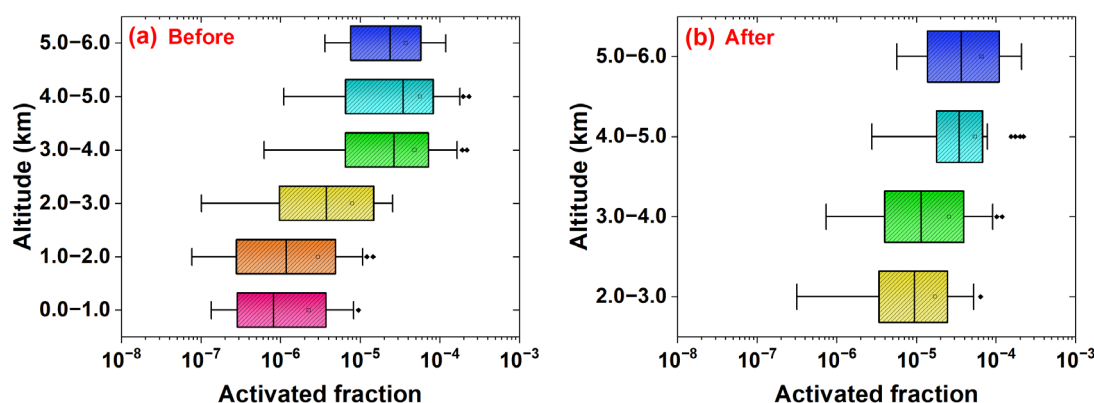
Figure 10. The activated fractions of total particles at different heights before (**a**) and after (**b**) the cold front passage. The box represents the interquartile.

3.4. Chemical Composition of INPs

Elemental compositions and morphology of the identified INPs (N = 93) were characterized using ESEM with energy dispersive spectrometer (ESEM-EDS). The categorized chemical composition of INPs is shown in Figure 11. INPs containing biogenic components have the smallest proportion. INPs containing mineral dust components (pure or mixed with other components) constitute the majority of total INPs, accounting for 76.1% and 89.2% before and after the passage of the cold front, respectively. Meanwhile, the proportion of pure mineral dust declines after the cold front passage, while the proportion of mineral dust mixed with other components increases. This suggests an increased probability of aging or coating of INPs introduced by the cold front during their long-distance transport.
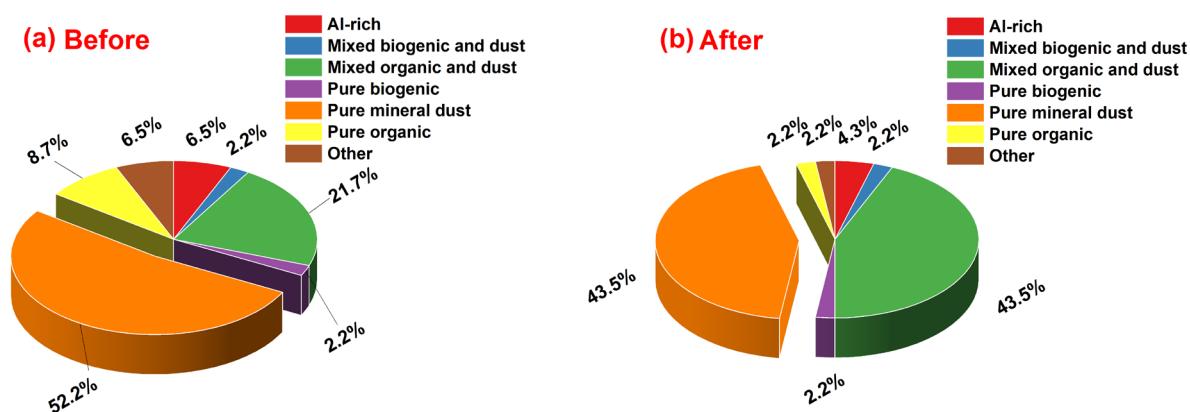
Figure 11. Chemical composition of identified INPs (N = 93) measured by ESEM-EDS before (**a**) and after (**b**) the cold front passage.

Figure 12 presents the size distribution of identified INPs collected at different heights. Despite the relatively low abundance of large aerosols at high altitudes, 88% of all INPs have a diameter exceeding 1 μm, making up the majority of INPs at high altitudes. After the cold front passage, 74% of INPs at the height of 4~6 km are giant aerosols (larger than 5 μm). These aerosols fall outside the measuring range (0.1–3 μm) of the onboard aerosol instrument (PCASP), which may explain the notably weak correlation between INP concentrations and aerosol concentrations. Furthermore, we found that, after the cold front passage, identified INPs tend to be larger compared to INPs sampled before the cold front passage. This could explain the higher concentration of INPs after the cold front passage, as larger particles can provide more activation sites for ice crystal formation.
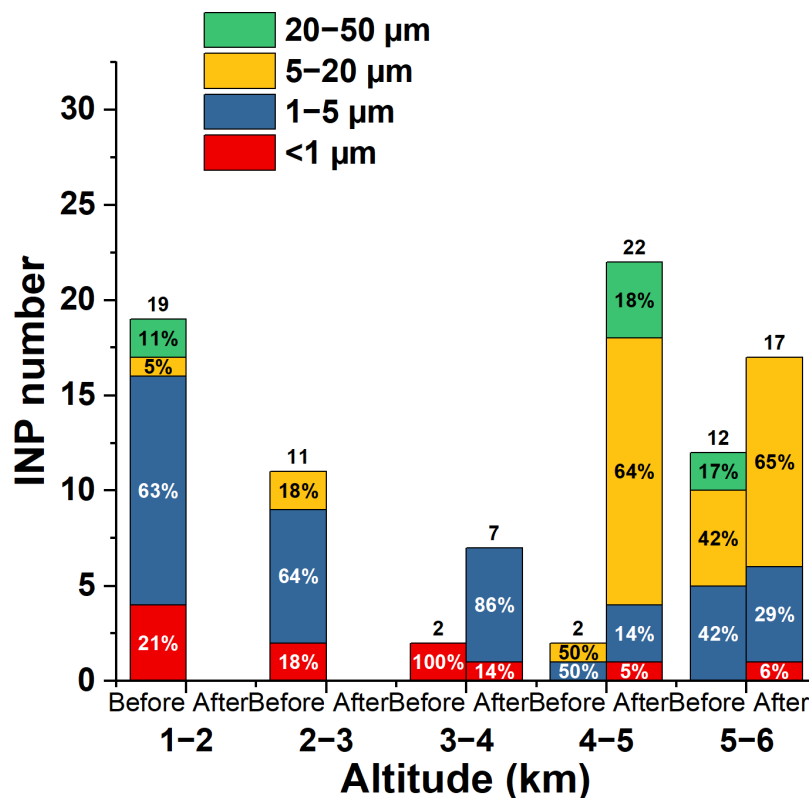

Figure 12. Size distribution of identified INPs (N = 93) collected at different heights before and after the cold front passage.

4. Discussion

In this study, the filter sampling method was used to measure INP concentrations, and the results were generally lower than those obtained using the continuous flow diffusion chamber (CFDC) [25,59,70]. Therefore, our results are closer to other observations that also used a filter sampling method. The INP concentrations measured in this study align well with the data reported by Jiang [48] (10^0–10^1 L^{-1}, ground-based observation in eastern China) and Niu [64] (0.29–0.93 L^{-1}, ground-based observation in northwestern China) and are slightly higher compared to the data presented by Chen [25] (10^{-3}–10^1 L^{-1}, ground-based observation in northern China). Schrod [71] reported higher INP concentrations (10^{-1}–10^2 L^{-1}) at heights ranging from 0.5 to 2.5 km using an unmanned aircraft system and FRIDGE cloud chamber. This difference can primarily be attributed to the presence of a desert dust layer at the 2 km height during their sampling periods.

The vertical mixing effect within the boundary layer is much stronger compared to the upper troposphere due to the influence of the underlying surface, resulting in greater uncertainty in the vertical distribution of INPs within the boundary layer [56]. Aircraft observations in India showed that INP concentrations were higher at heights below 3 km [59], which is consistent with our results (observation before the cold front passage). Previous studies have also highlighted notable regional disparities in the vertical distribution of INP concentrations [56–66].

Due to the low abundance of INPs in the atmosphere, establishing a sufficiently extensive observational database for INPs in the actual atmosphere to facilitate INP classification is difficult [30]. A key challenge is the difficulty in isolating INPs from a multitude of aerosol particles for subsequent individual chemical composition analysis. Here, we employed a well-established method to identify INPs in the ESEM system for further chemical analysis. However, this method also has its limitations. First, we needed to place the samples in the ESEM system and manually search for INPs based on the coordinates of ice crystals. Therefore, it is not feasible to generate a large amount of data about the INPs. Secondly, if more than one particle was present at a location where ice crystals have appeared, we were unable to identify which one is the INP. Therefore, the database of identified INPs is limited (93 in total). The current limitations necessitate the development of more intelligent and autonomously functioning systems to identify INPs in ESEM or other SEM systems in future studies. Additionally, to avoid excessively high aerosol density on the substrate, careful consideration should be given to the volume of air pumped for aerosol collection intended for INP chemical analysis.

Previous field observations, especially those conducted at high altitudes, highlighted the diverse composition of atmospheric INPs [59]. Particles originating from the near surface can be lifted to higher altitudes due to convective mixing and then transported to other remote regions via long-distance transport. The aging and mixing processes they undergo in the atmosphere can significantly modify their physical and chemical properties, as well as their ice-nucleating capacities [37]. In this study, we found that after the cold front passage, the proportion of pure mineral dust declines, while the proportion of mineral dust mixed with other components increases. Some previous studies have shown that, in comparison to pristine dust particles, dust particles coated with organic and biogenic constituents exhibit almost the same ice-nucleating capacities under the same activation conditions [26,72]. However, we are unable to conclude whether the dust particles mixed with other components exhibit higher or lower ice-nucleating capacity compared to pristine dust, because we don't have samples collected from the dust source region for comparison in this study. Furthermore, the degree of internal and external mixing remains uncertain, requiring extensive further research to quantitatively assess the detailed contributions of different chemical components to the activation of INPs.

5. Conclusions

In this study, we conducted aircraft observations over the North China Plain before and after a cold front passage to explore the impact of transport events on the vertical

distribution of INPs. A well-established method was employed to identify INPs and to perform single-particle chemical composition analysis using the ESEM-EDS system.

Within the activation temperature range of $-20 \sim -29\,^{\circ}\mathrm{C}$, the INP concentrations varied from 0.1 to 9.2 L^{-1}. The observed INP concentrations had a decreasing trend with height before the cold front passage. However, the highest INP concentration value appeared at higher altitudes (4~5 km) after the cold front passage. The cold front passage modified the distribution of INP concentrations but had limited impact on the vertical distribution of aerosols. This led to weakened correlations between INP and aerosol concentrations after the cold front passage. Furthermore, the increase in activated fraction with altitude indicated stronger ice-nucleating capacities of aerosols at higher altitudes, despite lower concentration of total particles compared to near ground.

Elemental and morphology analysis suggested that the INPs containing mineral dust components were the major contributors to total INPs. The proportion of mineral dust mixed with other components increased after the cold front passage. This indicated that the probability of aging or coating of INPs introduced by the cold front increased during long-distance transport. Furthermore, the INPs tend to be larger compared to those sampled before the cold front passage. During both flights, 88% of the total identified INPs had a diameter exceeding 1 μm, indicating that larger aerosols accounted for the predominant fraction of INPs at high altitudes.

Our study provides insights into the INPs' profiles and emphasizes the influence of transport events on the concentrations and sources of high-altitude INPs over Northern China. Note that this study only focuses on a case of cold front passage, and further observations are needed to draw more generalized conclusions regarding the INPs characteristics in China and to enrich the global database of the INP profiles.

References

1. Vali, G.; DeMott, P.J.; Möhler, O.; Whale, T.F. Technical Note: A proposal for ice nucleation terminology. *Atmos. Chem. Phys.* **2015**, *15*, 10263–10270. [CrossRef]
2. Lohmann, U.; Lüönd, F.; Mahrt, F. *An Introduction to Clouds: From the Microscale to Climate*; Cambridge University Press: Cambridge, UK, 2016; pp. 167–182.
3. Pruppacher, H.R.; Klett, J.D. *Microphysics of Clouds and Precipitation: With an Introduction to Cloud Chemistry and Cloud Electricity*; ProQuest: Ringwood, UK, 1997; p. 954.
4. Marcolli, C. Deposition nucleation viewed as homogeneous or immersion freezing in pores and cavities. Atmos. *Chem. Phys.* **2014**, *14*, 2071–2104.
5. Lohmann, U. *Aerosol-Cloud Interactions and Their Radiative Forcing, Encyclopedia of Atmospheric Sciences*; Elsevier Academic Press: Amsterdam, The Netherlands, 2015; pp. 17–22.
6. Zhu, J.; Penner, J.E. Radiative forcing of anthropogenic aerosols on cirrus clouds using a hybrid ice nucleation scheme. *Atmos. Chem. Phys.* **2020**, *20*, 7801–7827. [CrossRef]
7. Zhu, J.; Penner, J.E. Indirect Effects of Secondary Organic Aerosol on Cirrus Clouds. *J. Geophys. Res. Atmos.* **2020**, *125*, e2019JD032233. [CrossRef]
8. Rosenfeld, D.; Woodley, W.L. Closing the 50-year circle: From cloud seeding to space and back to climate change through precipitation physics. *Meteorol. Monogr.* **2003**, *51*, 59–80. [CrossRef]

9. Zhao, X.; Liu, X.; Burrows, S.M.; Shi, Y. Effects of marine organic aerosols as sources of immersion-mode ice-nucleating particles on high-latitude mixed-phase clouds. *Atmos. Chem. Phys.* **2021**, *21*, 2305–2327. [CrossRef]

10. Zhao, B.; Wang, Y.; Gu, Y.; Liou, K.-N.; Jiang, J.H.; Fan, J.; Liu, X.; Huang, L.; Yung, Y.L. Ice nucleation by aerosols from anthropogenic pollution. *Nat. Geosci.* **2019**, *12*, 602–607. [CrossRef]

11. Vergara-Temprado, J.; Miltenberger, A.K.; Furtado, K.; Grosvenor, D.P.; Shipway, B.J.; Hill, A.A.; Wilkinson, J.M.; Field, P.R.; Murray, B.J.; Carslaw, K.S. Strong control of Southern Ocean cloud reflectivity by ice-nucleating particles. *Proc. Natl. Acad. Sci. USA* **2018**, *115*, 2687–2692. [CrossRef]

12. DeMott, P.J.; Prenni, A.J.; Liu, X.; Kreidenweis, S.M.; Petters, M.D.; Twohy, C.H.; Richardson, M.S.; Eidhammer, T.; Rogers, D.C. Predicting global atmospheric ice nuclei distributions and their impacts on climate. *Proc. Natl. Acad. Sci. USA* **2010**, *107*, 11217–11222. [CrossRef]

13. DeMott, P.J.; Möhler, O.; Cziczo, D.J.; Hiranuma, N.; Petters, M.D.; Petters, S.S.; Belosi, F.; Bingemer, H.G.; Brooks, S.D.; Budke, C.; et al. The Fifth International Workshop on Ice Nucleation phase 2 (FIN-02): Laboratory intercomparison of ice nucleation measurements. Atmos. *Chem. Phys.* **2018**, *11*, 6231–6257. [CrossRef]

14. Bundke, U.; Nillius, B.; Jaenicke, R.; Wetter, T.; Klein, H.; Bingemer, H. The fast Ice Nucleus chamber FINCH. *Atmos. Res.* **2008**, *90*, 180–186. [CrossRef]

15. Möhler, O.; Field, P.R.; Connolly, P.; Benz, S.; Saathoff, H.; Schnaiter, M.; Wagner, R.; Cotton, R.; Krämer, M.; Mangold, A.; et al. Efficiency of the deposition mode ice nucleation on mineral dust particles. *Atmos. Chem. Phys.* **2006**, *6*, 3007–3021. [CrossRef]

16. Möhler, O.; Adams, M.; Lacher, L.; Vogel, F.; Nadolny, J.; Ullrich, R.; Boffo, C.; Pfeuffer, T.; Hobl, A.; Weiß, M.; et al. The Portable Ice Nucleation Experiment (PINE): A new online instrument for laboratory studies and automated long-term field observations of ice-nucleating particles. *Atmos. Meas. Tech.* **2021**, *14*, 1143–1166. [CrossRef]

17. Rogers, D.C. Development of a continuous flow thermal gradient diffusion chamber for ice nucleation studies. *Atmos. Res.* **1988**, *22*, 149–181. [CrossRef]

18. Bingemer, H.; Klein, H.; Ebert, M.; Haunold, W.; Bundke, U.; Herrmann, T.; Kandler, K.; Müller-Ebert, D.; Weinbruch, S.; Judt, A.; et al. Atmospheric ice nuclei in the Eyjafjallajökull volcanic ash plume. *Atmos. Chem. Phys.* **2012**, *12*, 857–867. [CrossRef]

19. Jiang, H.; Yin, Y.; Su, H.; Shan, Y.; Gao, R. The characteristics of atmospheric ice nuclei measured at the top of Huangshan (the Yellow Mountains) in Southeast China using a newly built static vacuum water vapor diffusion chamber. *Atmos. Res.* **2015**, *153*, 200–208. [CrossRef]

20. Conen, F.; Henne, S.; Morris, C.E.; Alewell, C. Atmospheric ice nucleators active $\geq -12\ ^\circ$C can be quantified on PM10 filters. *Atmos. Meas. Tech.* **2012**, *5*, 321–327. [CrossRef]

21. Chen, J.; Wu, Z.; Augustin-Bauditz, S.; Grawe, S.; Hartmann, M.; Pei, X.; Liu, Z.; Ji, D.; Wex, H. Ice-nucleating particle concentrations unaffected by urban air pollution in Beijing, China. *Atmos. Chem. Phys.* **2018**, *18*, 3523–3539. [CrossRef]

22. Schneider, J.; Höhler, K.; Heikkilä, P.; Keskinen, J.; Bertozzi, B.; Bogert, P.; Schorr, T.; Umo, N.S.; Vogel, F.; Brasseur, Z.; et al. The seasonal cycle of ice-nucleating particles linked to the abundance of biogenic aerosol in boreal forests. *Atmos. Chem. Phys.* **2021**, *21*, 3899–3918. [CrossRef]

23. Rzesanke, D.; Nadolny, J.; Duft, D.; Müller, R.; Kiselev, A.; Leisner, T. On the role of surface charges for homogeneous freezing of supercooled water microdroplets. Phys. *Chem. Chem. Phys.* **2012**, *14*, 9359–9363. [CrossRef]

24. Diehl, K.; Debertshäuser, M.; Eppers, O.; Schmithüsen, H.; Mitra, S.K.; Borrmann, S. Particle surface area dependence of mineral dust in immersion freezing mode: Investigations with freely suspended drops in an acoustic levitator and a vertical wind tunnel. *Atmos. Chem. Phys.* **2014**, *14*, 12343–12355. [CrossRef]

25. Hiranuma, N.; Augustin-Bauditz, S.; Bingemer, H.; Budke, C.; Curtius, J.; Danielczok, A.; Diehl, K.; Dreischmeier, K.; Ebert, M.; Frank, F.; et al. A comprehensive laboratory study on the immersion freezing behavior of illite NX particles: A comparison of 17 ice nucleation measurement techniques. *Atmos. Chem. Phys.* **2015**, *15*, 2489–2518. [CrossRef]

26. Kanji, Z.A.; Ladino, L.A.; Wex, H.; Boose, Y.; Burkert-Kohn, M.; Cziczo, D.J.; Krämer, M. Overview of Ice Nucleating Particles. *Meteorol. Monogr.* **2017**, *58*, 1.1–1.33. [CrossRef]

27. Hoose, C.; Möhler, O. Heterogeneous ice nucleation on atmospheric aerosols: A review of results from laboratory experiments. *Atmos. Chem. Phys.* **2012**, *12*, 9817–9854. [CrossRef]

28. Murray, B.J.; O'Sullivan, D.; Atkinson, J.D.; Webb, M.E. ChemInform Abstract: Ice Nucleation by Particles Immersed in Supercooled Cloud Droplets. *ChemInform* **2012**, *43*, 6519–6554. [CrossRef]

29. Cornwell, G.C.; McCluskey, C.S.; Levin, E.J.T.; Suski, K.J.; DeMott, P.J.; Kreidenweis, S.M.; Prather, K.A. Direct Online Mass Spectrometry Measurements of Ice Nucleating Particles at a California Coastal Site. *J. Geophys. Res. Atmos.* **2019**, *124*, 12157–12172. [CrossRef]

30. Cziczo, D.J.; Froyd, K.D.; Hoose, C.; Jensen, E.J.; Diao, M.; Zondlo, M.A.; Smith, J.B.; Twohy, C.H.; Murphy, D.M. Clarifying the dominant sources and mechanisms of cirrus cloud formation. *Science* **2013**, *340*, 1320–1324. [CrossRef]

31. Kanji, Z.A.; Abbatt, J.P.D. Ice nucleation onto Arizona test dust at cirrus temperatures: Effect of temperature and aerosol size on onset relative humidity. *J. Phys. Chem. A* **2010**, *114*, 935–941. [CrossRef]

32. Archuleta, C.M.; DeMott, P.J.; Kreidenweis, S.M. Ice nucleation by surrogates for atmospheric mineral dust and mineral dust/sulfate particles at cirrus temperatures. *Atmos. Chem. Phys.* **2005**, *5*, 2617–2634. [CrossRef]

33. Conen, F.; Rodríguez, S.; Glin, C.H.; Henne, S.; Herrmann, E.; Bukowiecki, N.; Alewell, C. Atmospheric ice nuclei at the high-altitude observatory Jungfraujoch, Switzerland. *Tellus B Chem. Phys. Meteorol.* **2022**, *67*, 25014. [CrossRef]

34. O'Sullivan, D.; Adams, M.P.; Tarn, M.D.; Harrison, A.D.; Vergara-Temprado, J.; Porter, G.C.E.; Holden, M.A.; Sanchez-Marroquin, A.; Carotenuto, F.; Whale, T.F.; et al. Contributions of biogenic material to the atmospheric ice-nucleating particle population in North Western Europe. *Sci. Rep.* **2018**, *8*, 13821. [CrossRef]

35. Wex, H.; Huang, L.; Zhang, W.; Hung, H.; Traversi, R.; Becagli, S.; Sheesley, R.J.; Moffett, C.E.; Barrett, T.E.; Bossi, R.; et al. Annual variability of ice-nucleating particle concentrations at different Arctic locations. *Atmos. Chem. Phys.* **2019**, *19*, 5293–5311. [CrossRef]

36. Gong, X.; Wex, H.; van Pinxteren, M.; Triesch, N.; Fomba, K.W.; Lubitz, J.; Stolle, C.; Robinson, T.-B.; Müller, T.; Herrmann, H.; et al. Characterization of aerosol particles at Cabo Verde close to sea level and at the cloud level—Part 2: Ice-nucleating particles in air, cloud and seawater. *Atmos. Chem. Phys.* **2020**, *20*, 1451–1468. [CrossRef]

37. Després, V.R.; Huffman, J.A.; Burrows, S.M.; Hoose, C.; Safatov, A.S.; Buryak, G.; Fröhlich-Nowoisky, J.; Elbert, W.; Andreae, M.O.; Pöschl, U.; et al. Primary biological aerosol particles in the atmosphere: A review. *Tellus B Chem. Phys. Meteorol.* **2022**, *64*, 15598. [CrossRef]

38. Knopf, D.A.; Alpert, P.A.; Wang, B. The Role of Organic Aerosol in Atmospheric Ice Nucleation: A Review. *ACS Earth Space Chem.* **2018**, *2*, 168–202. [CrossRef]

39. Phillips, V.T.J.; DeMott, P.J.; Andronache, C.; Pratt, K.A.; Prather, K.A.; Subramanian, R.; Twohy, C. Improvements to an Empirical Parameterization of Heterogeneous Ice Nucleation and Its Comparison with Observations. *J. Atmos. Sci.* **2013**, *70*, 378–409. [CrossRef]

40. Mahrt, F.; Alpert, P.A.; Dou, J.; Grönquist, P.; Arroyo, P.C.; Ammann, M.; Lohmann, U.; Kanji, Z.A. Aging induced changes in ice nucleation activity of combustion aerosol as determined by near edge X-ray absorption fine structure (NEXAFS) spectroscopy. *Environ. Sci. Process. Impacts* **2020**, *22*, 895–907. [CrossRef]

41. Mahrt, F.; Marcolli, C.; David, R.O.; Grönquist, P.; Barthazy Meier, E.J.; Lohmann, U.; Kanji, Z.A. Ice nucleation abilities of soot particles determined with the Horizontal Ice Nucleation Chamber. *Atmos. Chem. Phys.* **2018**, *18*, 13363–13392. [CrossRef]

42. Jahl, L.G.; Brubaker, T.A.; Polen, M.J.; Jahn, L.G.; Cain, K.P.; Bowers, B.B.; Fahy, W.D.; Graves, S.; Sullivan, R.C. Atmospheric aging enhances the ice nucleation ability of biomass-burning aerosol. *Sci. Adv.* **2021**, *7*, eabd3440. [CrossRef]

43. Zhang, Y.; Yu, F.; Luo, G.; Fan, J.; Liu, S. Impacts of long-range-transported mineral dust on summertime convective cloud and precipitation: A case study over the Taiwan region. *Atmos. Chem. Phys.* **2021**, *21*, 17433–17451. [CrossRef]

44. Burrows, S.M.; McCluskey, C.S.; Cornwell, G.; Steinke, I.; Zhang, K.; Zhao, B.; Zawadowicz, M.; Raman, A.; Kulkarni, G.; China, S.; et al. Ice-Nucleating Particles That Impact Clouds and Climate: Observational and Modeling Research Needs. *Rev. Geophys.* **2022**, *60*, 121. [CrossRef]

45. Chou, C.; Stetzer, O.; Weingartner, E.; Jurányi, Z.; Kanji, Z.A.; Lohmann, U. Ice nuclei properties within a Saharan dust event at the Jungfraujoch in the Swiss Alps. *Atmos. Chem. Phys.* **2011**, *11*, 4725–4738. [CrossRef]

46. DeMott, P.J.; Prenni, A.J.; McMeeking, G.R.; Sullivan, R.C.; Petters, M.D.; Tobo, Y.; Niemand, M.; Möhler, O.; Snider, J.R.; Wang, Z.; et al. Integrating laboratory and field data to quantify the immersion freezing ice nucleation activity of mineral dust particles. *Atmos. Chem. Phys.* **2015**, *15*, 393–409. [CrossRef]

47. Stith, J.L.; Ramanathan, V.; Cooper, W.A.; Roberts, G.C.; DeMott, P.J.; Carmichael, G.; Hatch, C.D.; Adhikary, B.; Twohy, C.H.; Rogers, D.C.; et al. An overview of aircraft observations from the Pacific Dust Experiment campaign. *J. Geophys. Res.* **2009**, *114*, 833. [CrossRef]

48. Jiang, H.; Yin, Y.; Wang, X.; Gao, R.; Yuan, L.; Chen, K.; Shan, Y. The measurement and parameterization of ice nucleating particles in different backgrounds of China. *Atmos. Res.* **2016**, *181*, 72–80. [CrossRef]

49. Jiang, H.; Yin, Y.; Chen, K.; Chen, Q.; He, C.; Sun, L. The measurement of ice nucleating particles at Tai'an city in East China. *Atmos. Res.* **2020**, *232*, 104684. [CrossRef]

50. Wgh, S.; Singh, P.; Ghude, S.D.; Safai, P.; Prabhakaran, T.; Kumar, P.P. Study of ice nucleating particles in fog-haze weather at New Delhi, India: A case of polluted environment. *Atmos. Res.* **2021**, *259*, 105693. [CrossRef]

51. Hu, Y.; Tian, P.; Huang, M.; Bi, K.; Schneider, J.; Umo, N.S.; Ullmerich, N.; Höhler, K.; Jing, X.; Xue, H.; et al. Characteristics of ice-nucleating particles in Beijing during spring: A comparison study of measurements between the suburban and a nearby mountain area. *Atmos. Environ.* **2023**, *293*, 119451. [CrossRef]

52. Bi, K.; Ma, X.; Chen, Y.; Fu, S.; Xue, H. The Observation of Ice-Nucleating Particles Active at Temperatures above—15 °C and Its Implication on Ice Formation in Clouds. *J. Meteorol. Res.* **2018**, *32*, 734–743. [CrossRef]

53. Bi, K.; McMeeking, G.R.; Ding, D.P.; Levin, E.J.T.; DeMott, P.J.; Zhao, D.L.; Wang, F.; Liu, Q.; Tian, P.; Ma, X.C.; et al. Measurements of Ice Nucleating Particles in Beijing, China. *J. Geophys. Res. Atmos.* **2019**, *124*, 8065–8075. [CrossRef]

54. Zhang, C.; Wu, Z.; Chen, J.; Chen, J.; Tang, L.; Zhu, W.; Pei, X.; Chen, S.; Tian, P.; Guo, S.; et al. Ice-nucleating particles from multiple aerosol sources in the urban environment of Beijing under mixed-phase cloud conditions. *Atmos. Chem. Phys.* **2022**, *22*, 7539–7556. [CrossRef]

55. Ren, Y.Z.; Bi, K.; Fu, S.Z.; Tian, P.; Huang, M.Y.; Zhu, R.H.; Xue, H.W. The Relationship of Aerosol Properties and Ice-Nucleating Particle Concentrations in Beijing. *J. Geophys. Res. Atmos.* **2023**, *128*, e2022JD037383. [CrossRef]

56. He, C.; Yin, Y.; Wang, W.; Chen, K.; Mai, R.; Jiang, H.; Zhang, X.; Fang, C. Aircraft observations of ice nucleating particles over the Northern China Plain: Two cases studies. *Atmos. Res.* **2021**, *248*, 105242. [CrossRef]

57. Hobbs, P.V. *Clouds: Their Formation, Optical Properties and Effects*; Academic Press: Washington, DC, USA, 1981; p. 497.

58. Rogers, D.C.; DeMott, P.J.; Kreidenweis, S.M. Airborne measurements of tropospheric ice-nucleating aerosol particles in the Arctic spring. *J. Geophys. Res.* **2001**, *106*, 15053–15063. [CrossRef]

59. Patade, S.; Nagare, B.; Wagh, S.; Maheskumar, R.S.; Prabha, T.V.; Pradeep Kumar, P. Deposition ice nuclei observations over the Indian region during CAIPEEX. *Atmos. Res.* **2014**, *149*, 300–314. [CrossRef]

60. Twohy, C.H.; McMeeking, G.R.; DeMott, P.J.; McCluskey, C.S.; Hill, T.C.J.; Burrows, S.M.; Kulkarni, G.R.; Tanarhte, M.; Kafle, D.N.; Toohey, D.W. Abundance of fluorescent biological aerosol particles at temperatures conducive to the formation of mixed-phase and cirrus clouds. *Atmos. Chem. Phys.* **2016**, *16*, 8205–8225. [CrossRef]

61. Conen, F.; Yakutin, M.; Yttri, K.; Hüglin, C. Ice Nucleating Particle Concentrations Increase When Leaves Fall in Autumn. *Atmosphere* **2017**, *8*, 202. [CrossRef]

62. Paul, S.K.; Sharma, S.K.; Selvam, A.M.; Murty, A.S.R. Aircraft observations of hygroscopic and ice-nuclei at a tropical station. *J. Rech. Atmos.* **1985**, *19*, 323–327.

63. Jiang, H.; Yin, Y.; Yang, L.; Yang, S.; Su, H.; Chen, K. The characteristics of atmospheric ice nuclei measured at different altitudes in the Huangshan Mountains in Southeast China. *Adv. Atmos. Sci.* **2014**, *31*, 396–406. [CrossRef]

64. Niu, S.J.; An, X.L.; Chen, Y.; Huang, S.H. 2000: Measurements and analysis of concentrations of atmospheric ice nuclei in the Helanshan area. *J. Nanjing Inst. Meteorol.* **2000**, *6*, 294–298.

65. Zhou, D.; Su, H.; Geng, S.; Wang, Y.; Hong, Y.; Liu, N. Aircraft observation of atmospheric ice nuclei concentration in Liaoning and Shenyang regions. *J. Meteorol. Environ.* **2018**, *34*, 133–139.

66. Wu, J.; Yin, Y.; Chen, K.; He, C.; Jiang, H.; Zheng, B.; Li, B.; Li, Y.; Lv, Y. Vertical Distribution of Atmospheric Ice Nucleating Particles in Winter over Northwest China Based on Aircraft Observations. *Atmosphere* **2022**, *13*, 1447. [CrossRef]

67. Schrod, J.; Danielczok, A.; Weber, D.; Ebert, M.; Thomson, E.S.; Bingemer, H.G. Reevaluating the Frankfurt isothermal static diffusion chamber for ice nucleation. *Atmos. Meas. Tech.* **2016**, *9*, 1313–1324. [CrossRef]

68. Su, H.; Yin, Y.; Lu, C.; Jiang, H.; Yang, L. Development of new diffusion cloud chamber type and its observation study of ice nuclei in the Huangshan area. *Chin. J. Atmos. Sci.* **2014**, *38*, 386–389.

69. Stein, A.F.; Draxler, R.R.; Rolph, G.D.; Stunder, B.J.B.; Cohen, M.D.; Ngan, F. NOAA's HYSPLIT Atmospheric Transport and Dispersion Modeling System. *Bull. Amer. Meteor. Soc.* **2015**, *96*, 2059–2077. [CrossRef]

70. López, M.L.; Ávila, E.E. Measurements of natural deposition ice nuclei in Córdoba, Argentina. *Atmos. Chem. Phys.* **2013**, *13*, 3111–3119. [CrossRef]

71. Schrod, J.; Weber, D.; Drücke, J.; Keleshis, C.; Pikridas, M.; Ebert, M.; Cvetković, B.; Nickovic, S.; Marinou, E.; Baars, H.; et al. Ice nucleating particles over the Eastern Mediterranean measured by unmanned aircraft systems. *Atmos. Chem. Phys.* **2017**, *17*, 4817–4835. [CrossRef]

72. Kanji, Z.A.; Sullivan, R.C.; Niemand, M.; DeMott, P.J.; Prenni, A.J.; Chou, C.; Saathoff, H.; Möhler, O. Heterogeneous ice nucleation properties of natural desert dust particles coated with a surrogate of secondary organic aerosol. *Atmos. Chem. Phys.* **2019**, *19*, 5091–5110. [CrossRef]